Available online at www.sciencedirect.com

jmr&t Journal of Materials Research and Technology

www.jmrt.com.br

Short Communication

Deep insight into the photoluminescent monocrystalline particles: Heat-treatment, structure, mechanisms and mechanics

Gözde Alkan[a,*,1], *HakanYavas*[b,c,1], *Berfu Göksel*[a,1], *Lidija Mancic*[d], *Bernd Friedrich*[a], *Olivera Milosevic*[d]

[a] *IME – Process Metallurgy and Metal Recycling, RWTH Aachen University, Aachen, Germany*
[b] *Department of Mechanical Engineering, Johns Hopkins University, Baltimore 21218, MD, USA*
[c] *Faculty of Electrical Engineering, Czech Technical University, KarlovoNamesti 13, Prague 4, Czech Republic*
[d] *Institute of Technical Sciences of Serbian Academy of Sciences and Arts, KnezMihailova 35, 11000 Belgrade, Serbia*

ARTICLE INFO

Article history:
Received 13 July 2018
Accepted 15 October 2018
Available online 11 January 2019

Keywords:
Rare earth oxides
Silver nanoparticles
Nanoindentation
Photoluminescence

ABSTRACT

The red light emitting down-converting Ag@Y_2O_3:Eu^{3+} phosphor particles were synthesized by one-step ultrasonic spray pyrolysis and exposed further to the heat treatment at 1000 °C (12 h). A detailed investigation on structural and functional properties of the as-prepared and heat treated particles was conducted in a comparative manner. High-resolution transmission electron microscopy (HRTEM), X-ray powder diffraction (XRPD) and focus ion beam milling (FIB) revealed in a great consistency the poorly crystallized and porous nature of the as-prepared particles. Well-crystallized coarser primary nanocrystals of Y_2O_3:$Eu^{3+}$and Ag, which are hierarchically organized in dense spherical Ag@Y_2O_3:Eu^{3+} phosphor particles, were obtained through the heat treatment. Along with the change of structural properties, down conversion (red luminescence at 612 nm owing to the $Eu^3 + {}^5D_0 \rightarrow {}^7F_2$ electric dipole transition) and mechanical endurance were enhanced 4-fold and 5-fold via heat treatment, respectively. This comparative study implies a good correlation between mechanical and luminescence behavior of phosphors, both strongly influenced by the particles structural properties.

1. Introduction

The demand for phosphor materials grows rapidly due to their extensive application in mobile phones, LED's, traffic displays and security markers [1–4]. Black banknotes and counterfeiting credit cards are becoming more threading and necessitate high efficient security inks which usually include a fluorescent component that could be activated with a ultraviolet or visible light for straightforward checking [5]. Metal-rare earth oxide nanostructures are considered as promising candidates for security ink applications owing to their superior luminescence efficiency, good corrosion resistance, high chemical and thermal stability [6–8]. Europium-doped yttrium oxide (Y_2O_3:Eu^{3+}), which is a down-converting phosphor that exhibit red-orange emission at 612 nm due to the ${}^5D_0 \rightarrow {}^7F_2$

* *Corresponding author.*
E-mail: galkan@ime-aachen.de (G. Alkan).
[1] These authors contributed equally to this work.

https://doi.org/10.1016/j.jmrt.2018.10.013

electric dipole transition of Eu^{3+}, is an indispensable candidate which possess excellent atmospheric stability, reduced degradation under applied voltages, high quantum efficiency and lack of hazardous constituents (unlike sulphide phosphors) [9,10]. The host lattice manipulation, energy transfer modulation, surface passivation, surface plasmon coupling, broadband sensitization, and photonic crystal engineering were recently reported as possible strategies that could even improve its luminescence response [11]. Among these, surface plasmon coupling has gained most attention due to the fact that noble metal nanoparticles (such as Au, Pt andAg) incorporated into oxide structure or present in close proximity of emitters enhances photoluminescence (PL) efficiency by energy transfer (ET) and local field enhancement (LCE) [12–14].

Ag incorporated Y_2O_3:Eu^{3+} synthesized by USP are chosen to be the focus of this study due to the superior PLA (when compared with Y_2O_3:Eu), as reported in [15]. The plasmon effect observed on the Ag nanoparticles [15] contributed to an increase of the relative luminescence intensity of Eu^{3+}-doped Y_2O_3 host lattice for about 34%, and could be enhanced more with the control of the particle morphology. There are various methods capable in producing hierarchically structured nanophosphors [16–21], however majority are challenging in terms of their cost efficiency and scale-up potential. Ultrasound assistant spray pyrolysis (USP) method is promising for the production of low-cost nanophosphors. In the USP process, the aerosol droplets experience evaporation/drying, precipitation and thermolysis in a single-step process under extreme synthesis conditions (high droplet/particle heating rate and high surface reactivity) resulting in the formation of spherical, hierarchically organized nanostructured particles through the mechanisms of primary nano crystals coalescence and collision [16,21]. However, due to fast reaction kinetics subsequent heat treatment may be required to improve particles crystallinity [22,23]. Since crystal quality, uniform distribution of constituents and defect concentration have direct influence on PL efficiency [24], and hence on mechanical properties too, it is intriguing to establish a correlation which will reveal uncovered features of PL using scalable and applicable system parameter, i.e. heat-treatment with nanoidentation for designing of the next-generation of efficient phosphors. Nanoindentation enables evaluation of mechanical properties in the small volume providing in such way precise detection of materials elastic and plastic behavior [25,26], which in turn could be correlated with some other property, in this case with the photoluminescence. However, it is worth to mention that measuring the single particle mechanical property is a challenging task which requires extra attention to exclude the contribution of the artificial deformation. There are only a few computational and experimental efforts [27–29] which can be used as guidance but the technical gap still remains.

Microstructural, PL and mechanical properties of as-prepared and heat treated Ag@Y_2O_3:Eu^{3+}particles synthesized by USP were elucidated in a comparative manner by HRTEM, XRPD, FIB, fluorescence measurement, and nanoindentation to establish an indirect relation between PL and mechanical properties. In brief, we "deeply" investigated structural properties of nanoparticles to reveal links at different length-scales, i.e. from atomic scale to microscale deformation for achieving glamorous PL properties.

2. Experimental procedure

Yttrium nitrate ($Y(NO_3)_3{\cdot}6H_2O$, Aldrich, purity >99%), europium nitrate ($Eu(NO_3)_3{\cdot}5H_2O$, Aldrich, purity >99%) and silver nitrate ($AgNO_3$, AppliChem, purity >98%) commercial precursors were used as yttrium oxide, europium, and silver precursors, respectively. The precursor solutions were prepared by dissolving relative amounts of nitrates, to obtain yttrium oxide doped with 5 at.% of Eu and decorated with 5 wt.% of Ag, in de-ionized water. Classical ultrasonic spray pyrolysis (USP) production line comprised ultrasound generator (1.7 MHz, Gapusol, RBI, France), a carrier gas (air) inlet connected over a flow regulator (1.5 l/min), horizontal wall heated furnace with a quartz tube and washing bottles for the collection of nanoparticles. Details of the experimental setup can be found elsewhere [30]. The precursoris atomized and carried by air to a heating zone, set at target temperature previously to experience evaporation, precipitation and thermal decomposition in a single-step. Synthesized product was exposed to post heat treatment at 1000 °C for 12 h in inert argon ambient to prevent the oxidation of silver.

The crystal structure of powders was elucidated by X-ray powder diffraction (XRPD) (Rigaku, 40 kV/40 mA). The patterns were recorded from 10° to 80° with a step scan of 0.02°/min and accounting time of 5 s per step. Refined structural data were evaluated through Rietveld analysis using Topas 4.2. software and starting from ICSD data 086813 and 044387 (for Y_2O_3 and Ag, respectively). The average crystallite size was calculated using volume weighted mean column height broadening modeled by a Voigt function. Conventional and High-resolution transmission electron microscopy (HRTEM) Jeol JEM-2100, Tecnai 20-F were used to reveal morphologic features and details of the microstructure. The chemical composition was determined using a Jeol JED-2300 Series energy 90 dispersive spectrometer (EDS). In addition, Gatan Digital Micrograph TM software was used to perform Fast Fourier Transformation (FFT) of the high-resolution transmission electron microscopy images (HRTEM) and confirmation of the crystal structure. In addition to the HRTEM analyses, we also performed scanning transmission electron microscopy (STEM) then cut the cross-sections of particles via Ga focused ion beam (FEI Helios Dual Beam STEM, CA) to reveal microstructural changes after heat-treatment. To do that, first, we choose an isolated particle to prevent plausible interactions with the neighbor particles and applied ion beam cross-cut at 52○ with a 30 kV accelerating voltage and 0.79 nA ion current. The photoluminescence spectra of the particles were recorded at room temperature by the Fluorescence Spectrophotometer FP-8600 (JASCO) with a scan rate of 200 nm/min and an excitation wavelength of 230 nm.

Nanoindentation load-sensitive experiments were performed with iNano (Nanomechanics Inc., TN) and Hysitron TI 950 (Hysitron Inc., MN) nanoindenters with a diamond Berkovich type. It should be noted that to eliminate possible oscillation based uncertainties, i.e. woodpecker effect, the dynamic force oscillation was disabled first and then indentations were carried out following quasi-static loading protocols.

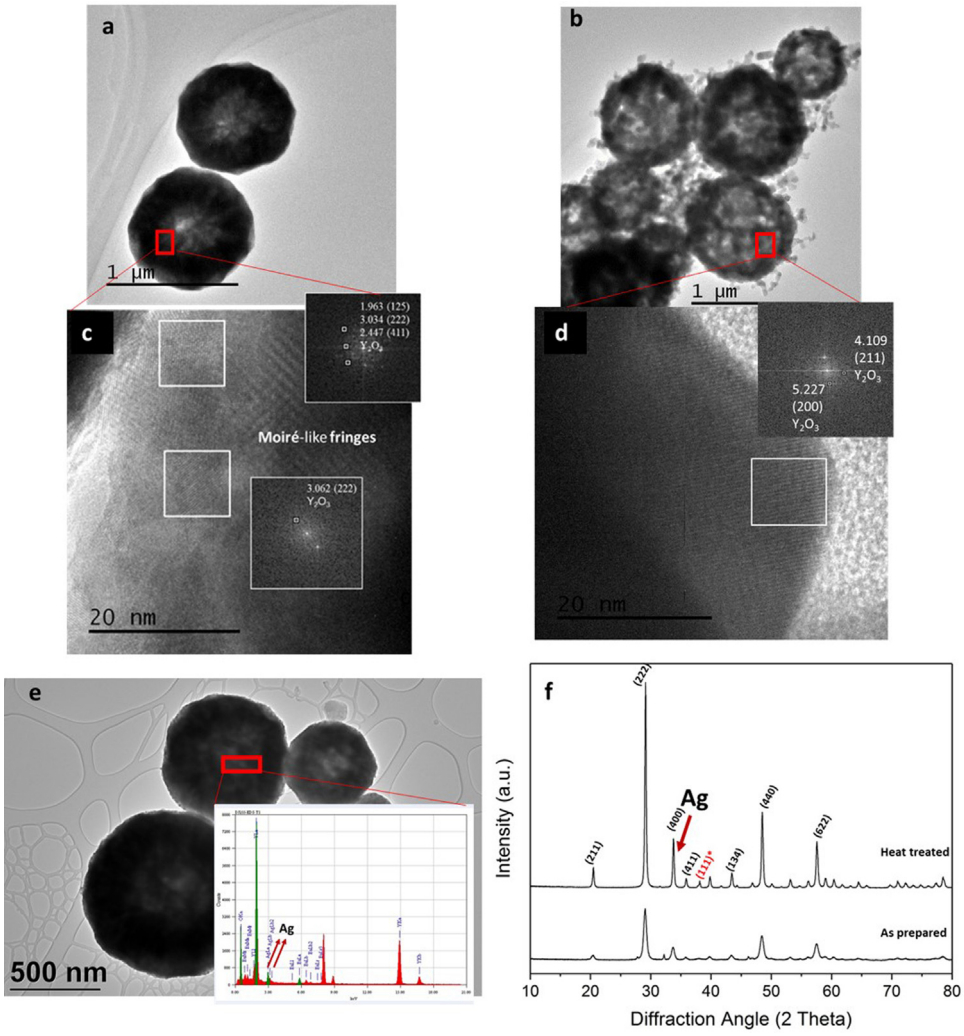

Fig. 1 – LRTEM micrographs of (a) as prepared, (b) heat treated samples and HRTEM micrographs with FFT analyses of (c) and (d), (e) EDX analyses of the as-prepared sample, (f) X-ray powder diffraction patterns of as-synthesized and heat treated samples in which Ag related (111) plane is marked with red *.

Prior to the indentations, an AFM like piezo-automated imaging mode was turned on to detect exact locations of particles with a scan rate of 1 Hz and 60 μm/s tip velocity. During the indentation, a constant strain rate loading was applied while keeping the depth at 500 nm. For the same depth level, each indent (total of 15 indentations) is displaced by 5 microns in all directions. Thermal drift was digitally monitored for the 20 s prior to each indentation and kept lower than 0.1 nm/s. All tests were performed at ambient conditions.

3. Results and discussion

Fig. 1a and b reveals low-resolution TEM (LRTEM) images of as prepared and heat-treated particles. Both samples exhibit typical USP spherical morphology assembled by fine primary crystals through collision/coalescence mechanism, as reported previously [22]. In as prepared particles, represented in Fig. 1a, a certain amount of porosity is detected, which is again consistent with previous studies. Since USP is a process with high heating/cooling rates (500 °C/s) and short reaction times (less than 1 s), reaction time does not allow completion of solid particle formation resulting in the porous microstructure. However, through the heat treatment, when extra time and heat provided for diffusion, the growth of primary particles results in the denser microstructure, as revealed in Fig. 1b.

During the formation of multicomponent structures via USP, all constituents experience evaporation, precipitation, and thermal decomposition simultaneously toward particle formation. Since europium and yttrium nitrate precursors have a low melting point (around 50 °C) and similar thermal decomposition mechanisms, their highly uniform distribution were achieved in the particles. However, $AgNO_3$ starts to experience thermal decomposition after these two constituents. Due to the differences in lattice parameters among the silver and the mentioned components and the consecutive precipitation, silver does not incorporate into the lattice of yttrium oxide, but rather precipitates on the surface of either primary or secondary Y_2O_3:Eu^{3+} particles forming a nanocomposite structure that might exhibit a plasmon effect

Table 1 – Refined structural parameters of the as-prepared and heat treated Ag@Y_2O_3:Eu^{3+}particles.

	As-prepared	Heat treated
Crystal structure	Cubic, *Ia-3*	Cubic, *Ia-3*
Unit cell parameter *a* (Å)	10.6248(5)	10.6193(1)
Crystallite size (nm)	16.5(3)	44.5(6)
OccY1 (C2)[a] OccY2 (S6)[a]	0.969 0.873	0.945 0.945
Strain	0.265(6)	0.090(2)
R_{Bragg}	1.962	1.123
GoF	1.266	1.148
RwP	7.884	6.456
Y1:O (Å)	2.2101(76)	2.2119(36)
Y2:O (Å)	2.3141(77)	2.2938(37)

[a] Occupation of C2 and S6 positions with Eu^{3+}could be calculated as 1-OccY1 and 1-OccY2, respectively.

on luminescence. Details of the formation mechanism of the multicomponent hierarchical systems obtained by USP can be found elsewhere [31]. Fig. 1 clearly supports the above statements. HRTEM images given in Fig. 1c and d highlights the details of both microstructures. Moiré like fringes and poorly organized structure were observed within the as-prepared particles, while after heat treatment well-crystalline particles free of defects were obtained. FFT analysis helps in elucidation of the crystal structure in selected regions. As one could see, both regions (insets in Fig. 1c, d) exhibited crystal planes of Y_2O_3 phase (JCPDS card 89-5591). However, EDX analysis (Fig. 1e) of the selected area imply the presence of silver inside the secondary as-prepared particle, presumably distributed either in between or on the surface of primary ytria particles. XRPD patterns of both samples presented in Fig. 1f additionally confirm HRTEM findings. Poorly crystallized as-prepared particles were transferred into particles with a higher crystallinity, as it is implied by sharper diffraction lines with a higher intensity in upper diffractogram. In the same diffractogram it is possible to observe one of the most intense Ag diffraction line, (111), suggesting lack of the Ag crystallization in the as-prepared samples. In order to confirm its presence in the as-prepared particles, EDX was performed. Structural parameters of both samples evaluated by Rietveld refinement are listed in Table 1.

Presented data implies that both samples crystallized in the BCC cubic structure with the space group *Ia-3*, JCPDS card 89-5591 [32]. Increased lattice parameters of the Y_2O_3:Eu^{3+}phase detected in both samples implies that Eu^{3+}partially replaced Y^{3+} ions in the crystal lattice (lattice parameter of Y_2O_3 is 10.60 Å, ionic radii of $Eu^{3+}$and Y^{3+} ions are 0.947 and 0.90 Å respectively). Better and more homogeneous accommodation of Eu^{3+} ions are obtained in the heat treated particles. This is certain from the observed changes of following parameters: lattice parameter and microstrain decreased as a consequence of structural defect diminishing while equalization of the C2 and the S6 occupancy with the Y^{3+} ions is followed with a change of the Y-O bonds. Heat treatment provokes additional change in the crystallite size from 16.5 to 44.5 nm. Better particle crystallinity bring on microstrain reducing for more than 3 times. As it will be shown further all these affect luminescence emission efficiency through diminishing effect of quenching in Ag@Y_2O_3:Eu^{3+} heat treated sample.

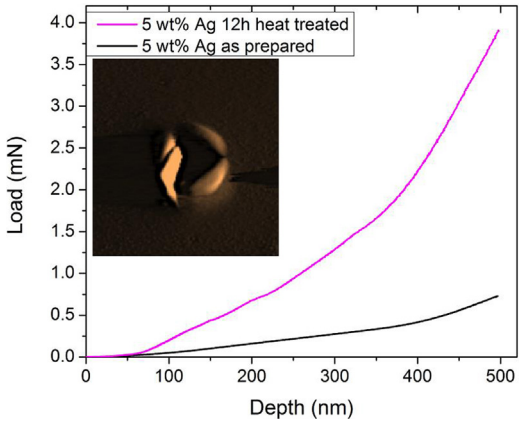

Fig. 2 – Nanoindentation load responses of the as-prepared and heat prepared particles. The inset shows the way of applying single particle indentation using the piezo-scanning method.

Fig. 2 shows the averaged load–responses of the as-prepared and heat treated samples. The inset presented in Fig. 2 demonstrates a representative piezo-automation image of indentation at the single particle. It is worth to mention that for the conventional nanoindentation, obtained hysteresis comprises three distinct regions: (i) loading, where the deformation is controlled by both elasticity and plasticity; (ii) dwell period/creep region; and (iii) elastic unloading. Since inter/intra-granular nature of the deformation might arise uncertainties during the unloading [25,26] we focused on the region i: level deformation loading in elasto-plastic region. At that stage, the resistive energy of the material will stop the motion of the nanoindenter tip at the predefined depth to underline the current mechanical state of the material. At this point, one can quantitatively extrapolate that the material with higher hardness will show superior load–response in comparison to its soft counterpart. As can be seen in Fig. 2, after particles heat treatment their load–response increased from 0.6 to 3.8 mN. Approximately 6 times higher load response obtained is a consequence of the better crystallinity, strain-free lattice and denser structure of the heat treated particle, confirmed through HRTEM and XRPD analyses.

Fig. 3a reveals excitation spectra of as prepared and heat treated samples, in a comparative manner. Due to the relatively lower excitation intensity of the as-prepared sample, its magnified view is given as inset in Fig. 3a. Y^{3+}–O^{2-} excitonic band at 210 nm and Eu^{3+}–O^{2-} charge transfer band at 250 nm (related to Eu^{3+} at C_2 position) are present in both spectra and are characteristic of the Eu^{3+} doped Y_2O_3 phase. The dramatic increase of the latter in the heat treated sample indicates an increasing rate of energy transfer between excited Eu^{3+} ions in C_2 and S_6 positions. The course of this transition is revealed through deconvolution and integration of the second peak in both spectra and obtained data implies that with heat treating Eu^{3+} ions migrate from S_6 to C_2, as it was shown through Rietveld refinement of the XRPD. It should be also noted that in the spectrum of the as-prepared sample additional band is visible at 314 nm. This may be due

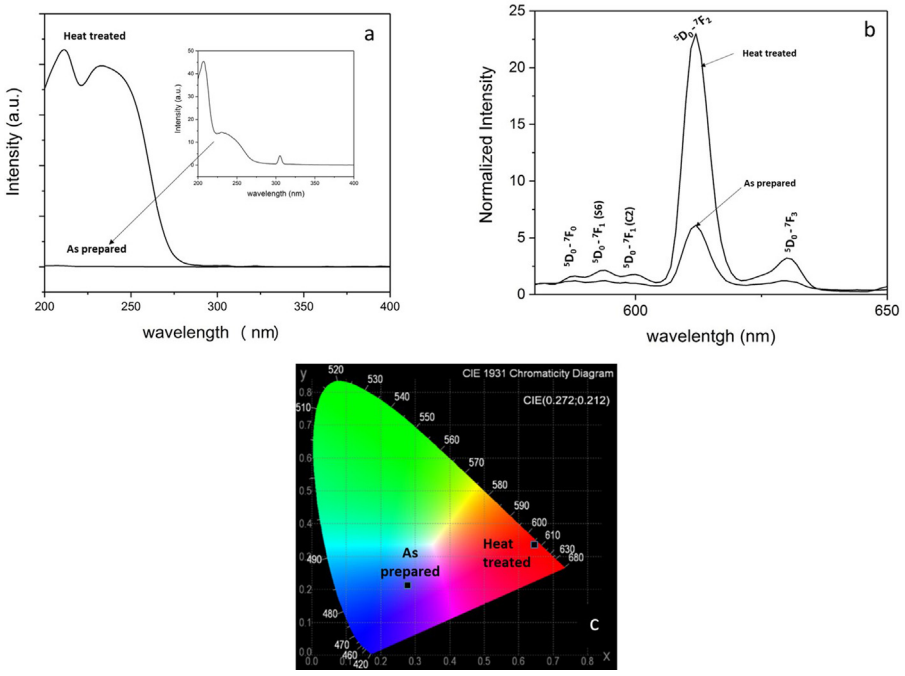

Fig. 3 – (a) Excitation spectra of samples, (b) emission spectra of samples excited by 230 nm and (c) corresponding CIE diagram revealing the visible color output.

to the excitation of Ag or due to the 4f–f transition of Eu^{3+} [33,34]. Fig. 3b represents the emission spectra of both samples excited at 230 nm. Typical red-light emission peak located at 612 nm is due to $^5D_0 \rightarrow {}^7F_2$transition of Eu^{3+} ions locating at the C_2 site. Since this peak is hypersensitive to local environment changes, it was considered as a comparison criterion between as prepared and heat-treatedsample which shows an approximately five-fold increase in emission intensity of the latter one. This enhancement in emission is in agreement with the improvement of the structural and specific crystallographic site occupation analysis. Since one of the most important properties of a phosphor is the purity of emitted color, CIE chromaticity coordinates X and Y were calculated for both samples, Fig. 3b. The chromaticity coordinates of (0.27, 0.21) and (0.64, 0.33) were obtained for the as prepared and heat treated samples, respectively. It is notable that color coordinates change dramatically with the heat treatment approaching the ideal red chromaticity defined by (0.67, 0.33) [35]. This indicates the feasibility of the USP synthesized particles to heat treatment for the target red-light-emitting phosphor applications.

To correlate the mechanical and luminescence properties of Y_2O_3:Eu^{3+}@Ag nanocomposite powders, structural data were used, as given in Fig. 4. As it was mentioned earlier during USP processing, droplet/particle residence time in the reaction zone was less than second, more precise 0.4 s. A high-temperature gradient was formed in the droplet instantly preventing the release of the gaseous product from decomposed precursor creating in that way porous particle structure or even the broken ones. Extremely short reaction time provokes nucleation of many interconnected primary particles with a poor crystallinity in a secondary spherical one. All that result in low mechanical endurance and weak luminescence emission. When additional heat treatment is applied, more uniform distribution of europium ion in Y_2O_3 matrix and almost complete neutralization of stress led to improving maximum load (5 fold) and red light emission (4 fold). In Fig. 4, the detailed microstructural analyses of the sample before (left) and after (right) heat treatment are presented revealing information from the particles inner structure. It highlights the fact that secondary spheres are really assembled from primary nanocrystals which size is consistent with ones

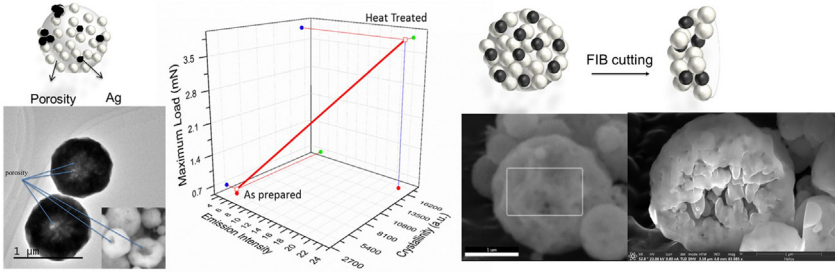

Fig. 4 – Correlation of emission intensity, crystallinity, and mechanical properties.

obtained through Rietveld refinement. Porosity present in the as-prepared particle (left) disappeared during annealing, so dense spherical particles composed form well crystallized primary ones were formed (right). Interconnected crystal islands which assemble the heat treated particle are responsible for the improved load response. Moreover, energy dispersive X-ray spectroscopy revealed a silver distribution on the surface of the primary Eu^{3+}-doped Y_2O_3 particles, amplifying their plasmonic effect on the luminescence.

4. Conclusion

In this study, the effect of heat treatment on hierarchically organized Y_2O_3:Eu^{3+}@Ag nanoparticles and their structural, mechanical and luminescence properties were reported. Local deformation characteristics and detailed structural analyses were correlated successfully with the photoluminescence efficiency of the particles. Detailed structural characterization revealed that poorly crystallized porous as-prepared particles obtained through USP were converted into highly crystallized dense ones with a uniform distribution of all constituents through additional heat treatment. Such particles emit red light which CIE coordinates (0.63, 0.33) are close to the pure red light (0.67, 0.33) and are characterized with the 5 fold enhancement in mechanical strength, so could be considered as an advanced phosphor nanocomposites that could be used in security ink applications.

Conflicts of interest

The authors declare no conflicts of interest.

Acknowledgments

Authors would like to thank CEITEC Research Infrastructure in Brno (CZ) and Johns Hopkins University (Maryland, USA) – Mechanical Engineering Department for the help with FIB and nanoindentation. We also like to thank Friedrich Rosen for his technical support in the laboratory and to Profs. Rebeka Rudolf, Satoshi Ohara, Sayaka Tamura, Koji Tomita, Zhenquan Tan, Fefei Sun and Rebeka Rudolf for their support in characterization. The support of Ministry of Education, Science and Technological Development, Republic of Serbia (Project #172035) is also kindly acknowledged.

REFERENCES

[1] Terraschke H, Wickleder C. UV, blue, green, yellow, red, and small: newest developments on Eu^{2+}-doped nanophosphors. Chem Rev 2015;115:11352–78.
[2] Kumar P, Dwivedi J, Gupta BK. Highly luminescent dual mode rare-earth nanorod assisted multi-stage excitable security ink for anti-counterfeiting applications. J Mater Chem C 2014;2:10468–75.
[3] Goldburt ET, Bhargava RN, Kulkarni BS. Method for producing rare earth activated metal oxide nanocrystals. U.S. Patent and Trademark Office; 1997; U.S. Patent No. 5,637,258. Washington, DC.
[4] Ferrer MM, de Santana YV, Raubach CW, La Porta FA, Gouveia AF, Longo E, et al. Europium doped zinc sulfide: a correlation between experimental and theoretical calculations. J Mol Model 2014;20:2375.
[5] Kaule W, Stenzel G. Security paper with authenticity features in the form of luminescing substances. U.S. Patent and Trademark Office; 1984; U.S. Patent No. 4,451,521. Washington, DC.
[6] Ćulubrk S, Lojpur V, Antić Z, Dramićanin MD. Structural and optical properties of europium doped Y_2O_3 nanoparticles prepared by self-propagation room temperature reaction method. J Res Phys 2014;37:39–45.
[7] Jayaramaiah J, Lakshminarasappa B, Nagabhushana B. Luminescence performance of europium-doped yttrium oxide thin films. J Lumin 2015;157:63–8.
[8] Jayaramaiah J, Lakshminarasappa B, Nagabhushana B. Luminescence studies of europium-doped yttrium oxide nano phosphor. Sensors Actuators B 2012;173:234–8.
[9] Taxak V, Khatkar S, Han S, Kumar R, Kumar M. Tartaric acid-assisted sol–gel synthesis of Y_2O_3:Eu^{3+} nanoparticles. J Alloys Comp 2009;469:224–8.
[10] FujiiK, Kitamoto Y, Hara M, Odawara O, Wada H. Optical properties of silica-coated Y_2O_3:Er,Yb nanoparticles in the presence of polyvinyl pyrrolidone. J Lumin 2014;156:8–15.
[11] Han S, Deng R, Xie X, Liu X. Enhancing luminescence in lanthanide-doped. Upconversion nanoparticles. Angew Chem Int Ed 2014;53:11702–15.
[12] Kassab LRP, Silva DS, Almeida R, Arauja CB. Photoluminescence enhancement by gold nanoparticles in Eu^{3+} doped GeO_2-Bi_2O_3 glasses. Appl Phys Lett 2009;94:101912.
[13] Inoue A, Fujii M, Sugimoto H, Imakita K. Surface plasmon-enhanced luminescence of silicon quantum dots in gold nanoparticle composites. J Phys Chem C 2015;119:25108–13.
[14] Wang Y, Zhou J, Wang T. Enhanced luminescence from the europium complex owing to surface plasmon resonance of silver nanoparticles. Mater Lett 2008;62:1937–40.
[15] Ferrari JL, Cebim MA, Pires AM, Coutodos Santos MA, Davolos MR. Y_2O_3:Eu^{3+} (5 mol%) with Ag nanoparticles prepared by citrate precursor. J Solid State Chem 2010;183:2110–5.
[16] Zhong S, Chen J, Wang S, Liu Q, Wang Y. Wang S.Y_2O_3:Eu^{3+} hexagonal microprisms: fast microwave synthesis and photoluminescence properties. J Alloys Comp 2010;493:322–5.
[17] Wu X, Tao Y, Gao F, Dong L, Hu Z. Preparation and photoluminescence of yttrium hydroxide and yttrium oxide doped with europium nanowires. J Cryst Growth 2005;277:643–9.
[18] Davolos MR, Feliciano S, Pires AM, Marques RF, Jafelicci M. Solvothermal method to obtain europium-doped yttrium oxide. J Solid State Chem 2003;171(1–2):268–72.
[19] Gupta BK, Haranath D, Saini S, Singh VN, Shanker V. Synthesis and characterization of ultra-fine Y_2O_3:Eu^{3+} nanophosphors for luminescent security ink applications. Nanotechnology 2010;21(5):055607.
[20] Park W, Lu D, Ahn S. Plasmon enhancement of luminescence upconversion. Chem Soc Rev 2015;44:2940–62.
[21] Lin H, Chen D, Yu Y, Shan Z, Huang P, Yang A, et al. A large red-shift in the photoluminescence emission of $Mg_{1-x}Sr_xTiO_3$. J Alloys Comp 2011;509:3363–6.
[22] Mancic L, Nikolic M, Gomez L, Rabanal ME, Milosevic O. Directed growth of nanoarchitected hybrid phosphor particles synthesized at low temperature. Adv Powder Technol 2014;25:1442–8.
[23] Marinkovic K, Mancic L, Gomez LS, Rabanal ME, Dramicanin M, Milosevic O. Photoluminescent properties of

nanostructured Y_2O_3:Eu^{3+} powders obtained through aerosol synthesis. Opt Mater 2010;32:1606–11.
[24] Prusty RK, Kuruva P, Ramamurty U, Thomas T. Correlations between mechanical and photoluminescence properties in Eu doped sodium bismuthtitanate. Solid StateCommun 2013;173:38–41.
[25] Schuh C. Nanoindentation studies of materials. Mater Today 2009;5:32–40.
[26] Yang PF, Chen DL, Jian SR, Lee SW, Tseng CJ. Mechanical properties of $Ba_{1-x}K_xCe_{0.6}Zr_{0.2}Y_{0.2}O_3$-δ Oxides by nanoindentation. Proc Eng 2014;79:599–605.
[27] Cao Y, Duan P, Chen J. Modelling the nanomechanical response of a micro particle–matrix system for nanoindentation tests. Nanotechnology 2016;27:195703.
[28] Lee S, Hong JY, Jang J. Performance enhancement of white light-emitting diodes using an encapsulant semi-solidification method. J Mater Chem C 2014;2:8525.
[29] Yan W, Pun CL, Simon GP. Conditions of applying Oliver–Pharr method to the nanoindentationof particles in composites. Comp Sci Technol 2012;72:1147–52.
[30] Bogovic J, Rudolf R, Friedrich B. The controlled single-step synthesis of Ag/TiO_2 and Au/TiO_2 by ultrasonic spray pyrolysis (USP). J Metals 2016;68:330.
[31] Alkan G, Rudolf R, Bogovic J, Jenko D, Friedrich B. Structure and formation model of Ag/TiO_2 and Au/TiO_2 nanoparticles synthesized through ultrasonic spray pyrolysis. Metals Open Access Metallur J 2017;7(10):389.
[32] Joint Committee on Powder Diffraction Standard, Diffraction Data File, Nos. 43-1036, 44-0399 and 04-0783. Pennsylvania: JCPDS International Center for Diffraction Data; 1991.
[33] Liu C, Yang X, Yuan H, Zhou Z, Xiao D. Preparation of silver nanoparticle and its application to the determination of ct-DNA. Sensors 2007;7:708–18.
[34] Binnemans K. Interpretation of europium(III) spectra. Coord Chem Rev 2015;295:1–45.
[35] Das SS, Dutta S, Visser HG, Pandey MK, Kumar P, Dubey RK, et al. Synthesis of strong red emitting Y_2O_3:Eu^{3+} phosphor by potential chemical routes: comparative investigations on the structural evolutions, photometric properties and Judd–Ofelt analysis. RSC Adv 2015;5:70887–98.